

# Extreme In-Plane Thermal Conductivity Anisotropy in Titanium Trisulfide Caused by Heat-Carrying Optical Phonons

Huili Liu,<sup>#</sup> Xiaoxia Yu,<sup>#</sup> Kedi Wu, Yang Gao, Sefaattin Tongay, Ali Javey, Lidong Chen,<sup>\*</sup> Jiawang Hong,<sup>\*</sup> and Junqiao Wu<sup>\*</sup>

Cite This: *Nano Lett.* 2020, 20, 5221–5227

Read Online

ACCESS |

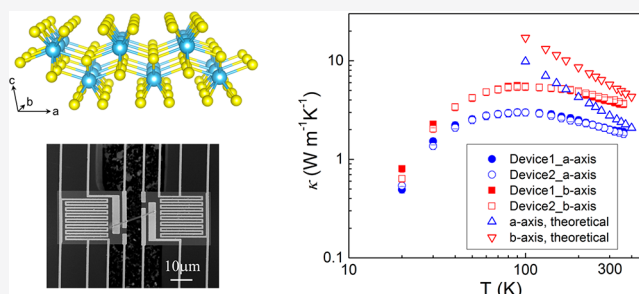
Metrics & More

Article Recommendations

Supporting Information

**ABSTRACT:** High in-plane anisotropies arise in layered materials with large structural difference along different in-plane directions. We report an extreme case in layered  $\text{TiS}_3$ , which features tightly bonded atomic chains along the  $b$ -axis direction, held together by weaker, interchain bonding along the  $a$ -axis direction. Experiments show thermal conductivity along the chain twice as high as between the chain, an in-plane anisotropy higher than any other layered materials measured to date. We found that in contrast to most other materials, optical phonons in  $\text{TiS}_3$  conduct an unusually high portion of heat (up to 66% along the  $b$ -axis direction). The large dispersiveness of optical phonons along the chains, contrasted to many fewer dispersive optical phonons perpendicular to the chains, is the primary reason for the observed high anisotropy in thermal conductivity. The finding discovers materials with unusual thermal conduction mechanism, as well as provides new material platforms for potential heat-routing or heat-managing devices.

**KEYWORDS:** Titanium trisulfide, in-plane anisotropy, optical phonons, thermal conductivity



Layered materials are held together between layers via weak, van der Waals (vdW) interactions, whereas within each layer the atoms are bonded together by much stronger covalent bonding. They draw tremendous research attention by their fascinating physical properties as a new class of two-dimensional (2D) materials when thinned down to the monolayer. Potential applications of these materials are being investigated for fields ranging from electronics,<sup>1–3</sup> catalysis,<sup>4</sup> and photonics<sup>5,6</sup> to sensing<sup>7,8</sup> and thermoelectrics.<sup>9</sup> Not surprisingly, the weak interlayer vdW interactions combined with the strong intralayer covalent bonding may lead to high anisotropies in properties between the cross-plane and in-plane directions. Additionally, it has also been realized that there exists structural anisotropy within the basal plane of most layered materials, such as the difference in armchair (AC) and zigzag (ZZ) structures in black phosphorus (b-P),<sup>10,11</sup> black arsenic (b-As),<sup>12</sup> tin selenide (SnSe),<sup>13</sup> and graphene.<sup>14</sup> This would result in modest in-plane anisotropies in physical properties, offering potential applications that are not possible with isotropic materials.<sup>15</sup>

Recently, layered transition metal trichalcogenides (TMTCs),  $\text{MX}_3$  ( $M = \text{Zr}, \text{Ti}$ , and  $X = \text{S}, \text{Se}$ ), have become a focus of interest,<sup>16,17</sup> attributed mostly to their unique, quasi-one-dimensional (1D) chain structure in the basal plane.<sup>18,19</sup> Among them, titanium trisulfide ( $\text{TiS}_3$ ) has a direct bandgap of  $\sim 1.0$  eV,<sup>20,21</sup> and a high on/off ratio of  $\sim 7000$  when made into field effect transistors.<sup>22</sup> Experiments show distinct carrier

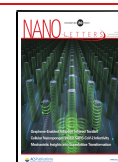
mobility of 80 and 40  $\text{cm}^2 \text{V}^{-1} \text{s}^{-1}$  along its  $b$ - and  $a$ -axis directions, respectively,<sup>23</sup> and an unusual sulfur–sulfur lone-pair vibrational mode of  $\text{TiS}_3$ .<sup>24</sup> However, an important physical property, thermal conductivity ( $\kappa$ ), has not been experimentally characterized in  $\text{TiS}_3$ , especially related to its unique quasi-1D chain structure in the basal plane. In this work, we report an extreme in-plane anisotropy in  $\kappa$  of  $\text{TiS}_3$  up to a ratio of 2, higher than any currently known layered materials, by combining advanced thermal transport measurements with first-principles calculations.

$\text{TiS}_3$  takes a monoclinic structure with the space group of  $P2_1/m$  ( $a = 4.96 \text{ \AA}$ ,  $b = 3.40 \text{ \AA}$ ,  $c = 8.79 \text{ \AA}$ ,  $\alpha = \gamma = 90^\circ$ ,  $\beta = 97.3^\circ$ ).<sup>25</sup> Figure 1a shows a schematic of the crystal structure of a single layer. Importantly, the basal plane features one-dimensional atomic chains along the  $b$ -axis direction, as shown in Figure 1b. The bonding lengths in the chain are 2.45 and 2.49  $\text{\AA}$ ,<sup>26</sup> slightly smaller than the sum of the individual covalent radii (1.05 and 1.60  $\text{\AA}$  for S and Ti,<sup>27</sup> respectively). The neighboring chains are laterally connected by longer Ti–S bonds along the  $a$ -axis, as shown in Figure 1c. These interchain

Received: April 8, 2020

Revised: June 15, 2020

Published: June 15, 2020



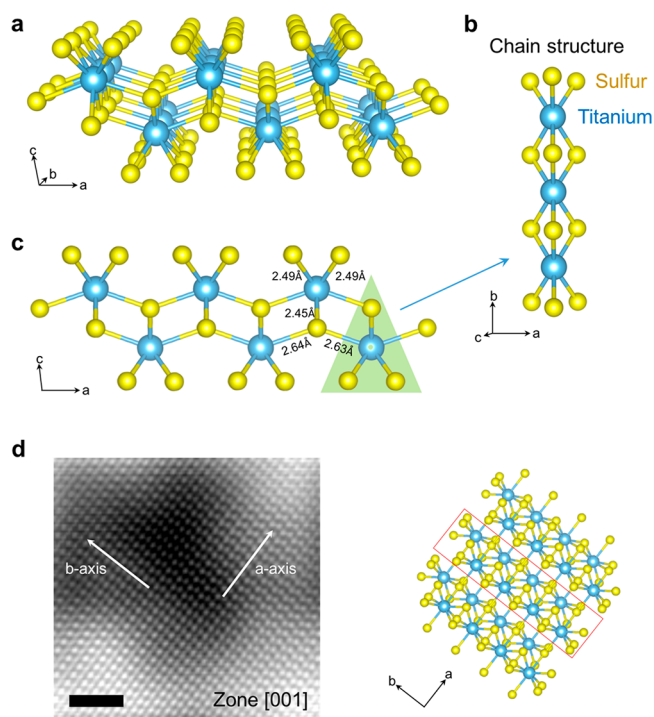


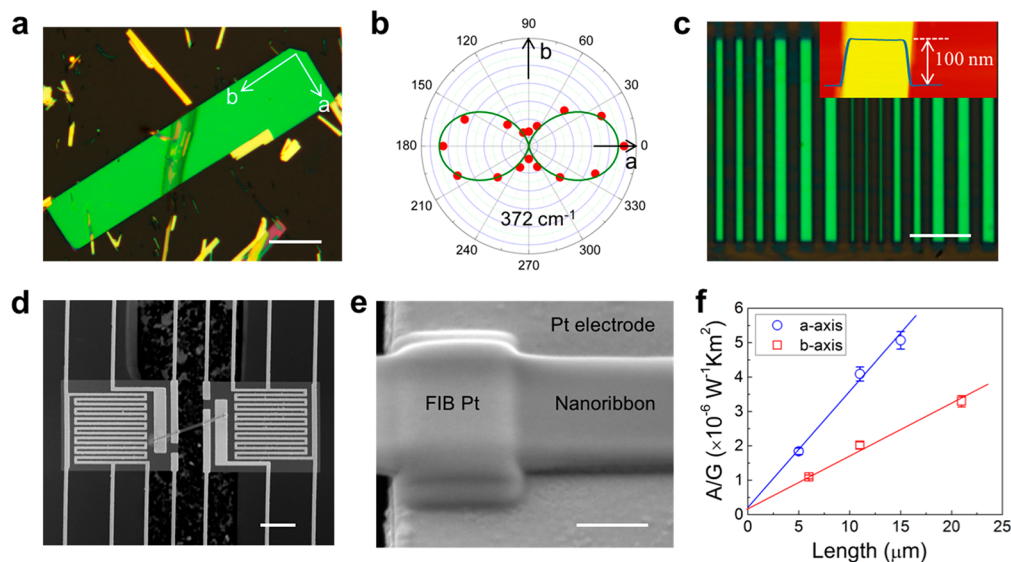
**Figure 1.** Crystal structure of  $\text{TiS}_3$ . (a) Monolayer of  $\text{TiS}_3$ . (b) Chain structure along the  $b$ -axis. (c) Side view of the monolayer. (d) TEM micrograph imaged along the  $c$ -axis (left) and the corresponding schematic structure (right). The red box indicates the chain along the  $b$ -axis. Scale bar, 1 nm.

bonding lengths are 2.63 and 2.64 Å, respectively, nearly equal to the sum of the individual covalent radii. This unique chain structure leads to high electronic, structural and vibrational

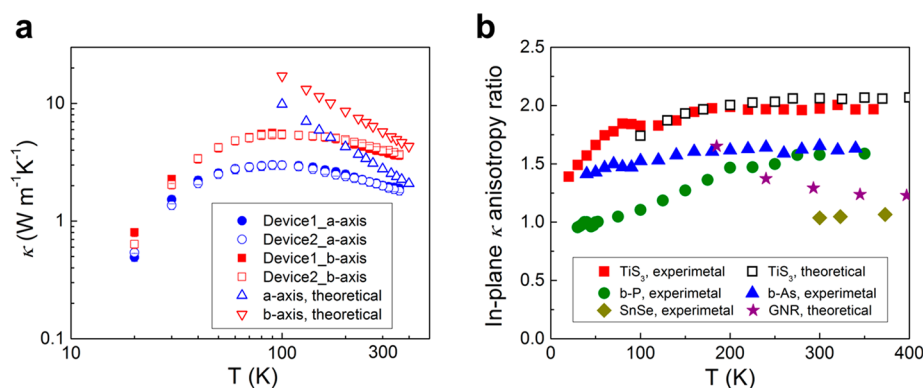
anisotropies in the basal plane of  $\text{TiS}_3$ . For the electronic structure, the  $3p_x$  orbitals of S atoms contribute mostly to the top of the valence band, which dominates the band dispersion along the  $a$ -axis direction; the  $3d_{x^2-y^2}$  orbitals of Ti atoms compose the conduction band, dispersing mostly along the  $b$ -axis direction.<sup>28</sup> Figure 1d is a high-resolution TEM (transmission electron microscopy) image of  $\text{TiS}_3$ , showing atomic arrangement along the  $a$ - and  $b$ -axis, consistent with the chain structures seen in the right panel.

Figure 2a shows a  $\text{TiS}_3$  flake mechanically exfoliated from the bulk crystal, where the crystallographic orientations were confirmed by micro-Raman analysis, as the Raman signal intensity depends on the angle between the laser polarization direction and the  $\text{TiS}_3$  crystal orientation.<sup>17</sup> Raman intensity of the most prominent peak<sup>17</sup> ( $372\text{ cm}^{-1}$ ) was fitted by theoretical angular dependence,  $I \propto \cos^2 \varphi$ , shown as a solid curve in Figure 2b, where  $\varphi = 0^\circ$  ( $90^\circ$ ) corresponds to the  $a$  ( $b$ )-axis direction of  $\text{TiS}_3$ . Details of device fabrication and measurements are in the Supporting Information.<sup>10,11</sup> Figure 2c shows a set of  $a$ -axis-oriented  $\text{TiS}_3$  nanoribbons of length  $\sim 40\ \mu\text{m}$  and width varying from 0.5 to  $2\ \mu\text{m}$ , e-beam lithographically patterned from a single flake with a thickness of 100 nm. The electrical contact of devices is improved by Pt deposition, as shown in Figure 2d,e, which results in negligible contact thermal resistance (Figure 2f) for the devices. All measurements were performed under high vacuum ( $<10^{-6}$  Torr) with a radiation shield.<sup>29–31</sup> The flexible and suspended nature of the device maximally releases any tensile, shearing, and torsional stress potentially built up in the nanoribbon, as well as eliminates substrate influence, during the measurements.

Figure 3a shows the temperature dependence of  $\kappa$  measured along the  $a$ - (defined as  $\kappa_a$ ) and  $b$ -axis ( $\kappa_b$ ) directions. It is found that  $\kappa_b$  is much higher than  $\kappa_a$  near room temperature,



**Figure 2.**  $\text{TiS}_3$  device fabrication for thermal and electrical measurements. (a) Optical image of exfoliated  $\text{TiS}_3$  flakes. (b) Angular dependence of the intensity of the  $A_g$  Raman mode at  $372\text{ cm}^{-1}$ . Solid curve is fitting to determine the crystal orientation along the  $a$ -axis and  $b$ -axis. (c) Optical image of lithographically patterned  $\text{TiS}_3$  nanoribbons. Inset is an AFM (atomic force microscopy) image that shows the thickness of 100 nm (error bar, 3 nm). (d) SEM (scanning electron microscopy) image of a suspended micropad device supporting a single nanoribbon. (e) SEM image of part of the nanoribbon Pt-bonded onto the underlying electrode by FIB (Focused Ion Beam). (f) Cross-sectional area/thermal conductance ( $A/G$ ) as a function of the nanoribbon length. Error bars include those from data of thermal conductance and sample size. These nanoribbons were made from the same flake (100 nm thick). The linear relation extrapolating to nearly zero indicates negligible thermal contact resistance for the measured nanoribbons devices. Scale bars:  $50\ \mu\text{m}$  (a);  $10\ \mu\text{m}$  (c), (d);  $500\ \text{nm}$  (e).



**Figure 3.** In-plane thermal conductivity ( $\kappa$ ) of  $\text{TiS}_3$  and its anisotropy. (a) Both measured and calculated temperature dependence of  $\kappa$  along the  $a$ - and  $b$ -axis. (b) In-plane anisotropy ratio of  $\kappa$ , defined as  $\kappa_b/\kappa_a$  for  $\text{TiS}_3$  (this work), compared to the same of  $\kappa_{ZZ}/\kappa_{AC}$  for b-P (170 nm thick nanoribbon, experimental), b-As (124 nm thick nanoribbon, experimental), SnSe (bulk, experimental), and graphene nanoribbon (GNR, theoretical).

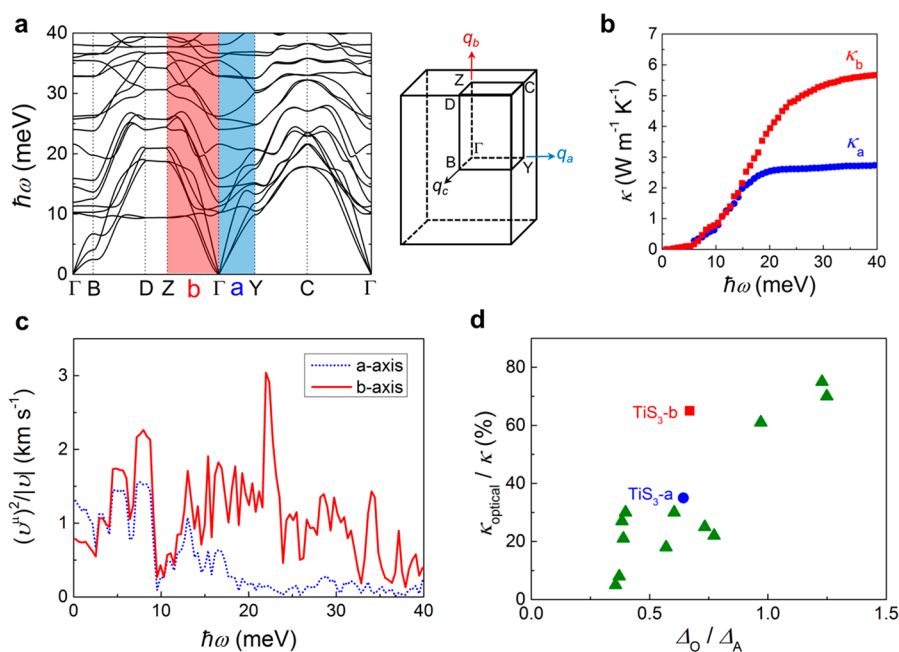


**Figure 4.** DFT calculation of phonon properties of  $\text{TiS}_3$ . (a) Phonon dispersion of  $\text{TiS}_3$ . The right panel shows the Brillouin zone of  $\text{TiS}_3$ . (b) Energy dependence of cumulative lattice thermal conductivity along the  $a$ - and  $b$ -axis at 300 K. (c) Average group velocity of phonon modes along the  $a$ - and  $b$ -axis, respectively, showing high anisotropy for optical phonons between 15 and 30 meV. (d) Calculated percentage of optical phonon contribution to total thermal conductivity, plotted as a function of bandwidth of the most dispersive optical phonon normalized by the bandwidth of acoustic phonons. The materials are listed in Table 1.

but they gradually become similar at lower temperatures. As shown in Figure 3b, the anisotropic ratio of  $\kappa$  ( $=\kappa_b/\kappa_a$ ) remains nearly a constant of 2.0 between  $T \approx 150$  and 360 K, but at  $T < 150$  K the ratio is reduced toward 1.4 at  $T \approx 20$  K. As a comparison, we show the in-plane anisotropy in  $\kappa$  of b-P,<sup>10</sup> b-As,<sup>12</sup> SnSe,<sup>13</sup> and graphene nanoribbon (GNR),<sup>32</sup> as they also possess structural anisotropy along their ZZ and AC directions in the basal plane. Their  $\kappa$  anisotropy ( $\kappa_{ZZ}/\kappa_{AC}$ ) at 300 K is 1.6 for b-P and b-As, 1.0 for SnSe, and 1.3 for GNR. It is clear that  $\text{TiS}_3$  hosts the highest in-plane anisotropy in  $\kappa$  compared to all other layered materials. Because the electrical conductivity of these  $\text{TiS}_3$  nanoribbons is very low, about 80 and 90  $\text{S m}^{-1}$  along the  $a$ - and  $b$ -axis at 300 K, respectively (Figure S3 in the Supporting Information), electronic contributions to  $\kappa$  is negligible, and the measured  $\kappa$  is therefore dominated by lattice thermal conductivity. Unlike the structural anisotropy arising

from the ZZ versus AC bonding in b-P, b-As, SnSe, and GNR, the quasi-1D chain structure of  $\text{TiS}_3$  is suspected to be responsible for this unusually high  $\kappa$  anisotropy in its basal plane.

To elucidate the physical mechanism of the anisotropic thermal conductivity in  $\text{TiS}_3$ , we calculated the phonon dispersion and thermal transport properties using density functional theory (DFT) and phonon Boltzmann transport equations via iterative solution within ShengBTE. Figure 4a shows the phonon dispersion of  $\text{TiS}_3$  along the  $\Gamma$ -Y ( $a$ -axis) and  $\Gamma$ -Z ( $b$ -axis) directions in the first Brillouin zone. These results are consistent with first-principles calculations of monolayer  $\text{TiS}_3$  reported by Zhang et al.<sup>33</sup>

The lattice thermal conductivity tensor, relating temperature gradient in the  $\nu$  direction to heat current per unit area in the  $\mu$  direction through Fourier's law, is a summation of contribu-



tions from all phonon modes ( $j$ ) over wavevectors ( $\mathbf{q}$ ) in the first Brillouin zone,<sup>34</sup> written as

$$\kappa_{\mu\nu} = \frac{1}{3} \sum_{\lambda} c_{\lambda} v_{\lambda,\mu} v_{\lambda,\nu} \tau_{\lambda} \quad (1)$$

where the index  $\lambda = j$ ,  $\mathbf{q}$ ,  $c_{\lambda}$  is specific heat capacity,  $v_{\lambda,\mu}$  is phonon group velocity in the  $\mu$  direction, and  $\tau_{\lambda}$  is phonon relaxation time. The first suspect that may cause the large anisotropy in  $\kappa$  would be anisotropy in acoustic phonon group velocity or anharmonicity, as demonstrated in the case of b-P.<sup>10</sup> However, from the dispersion relation in Figure 4a, it can be seen that the acoustic phonon group velocity does not differ significantly along the  $a$ - and  $b$ -axis directions. Indeed, as shown in Table S1 (see Supporting Information), the averaged group velocity of acoustic phonons is calculated to  $v_A = 4.44$  km s<sup>-1</sup> and 4.79 km s<sup>-1</sup> along the  $a$ - and  $b$ -axis, respectively. These values differ by only ~8%, or if comparing the velocity squared ( $v_A^2$ ), differ by only ~16%. This is far lower than the observed anisotropy in  $\kappa$  by a factor of 2. The anharmonicity of phonons is characterized by the Grüneisen parameter (1.91 and 1.06 simulated along the  $a$ - and  $b$ -axis at 300 K, respectively) and enables the typical three-phonon processes, which defines  $\tau_{\lambda}$  at temperatures higher than the Debye temperature. However, these phonon–phonon scattering processes sample phonon modes in all phase space that is allowed by energy conservation and the Umklapp momentum restriction, effectively mixing the lattice anharmonicity along all crystal directions. Therefore, we conclude that acoustic phonons are not the primary reason for the observed 2-fold in-plane anisotropy in  $\kappa$ .

We now focus on contributions from the optical phonons. First, we calculated the cumulative lattice thermal conductivity along  $a$ - and  $b$ -axis at 300 K as a function of phonon energy, taking into account all three-phonon scattering processes. The results are shown in Figure 4b, where  $\kappa_b$  is cumulated to 5.78 W m<sup>-1</sup> K<sup>-1</sup> and  $\kappa_a$  to 2.84 W m<sup>-1</sup> K<sup>-1</sup> (Table S2), giving rise to the theoretical anisotropy ratio of 2 in Figure 3b. At this temperature or higher ( $k_B T > 26$  meV), the optical phonons along both directions, having energies of 10–30 meV, are nearly fully thermally activated. More importantly, it is clear that for all phonon energies below 15 meV, i.e., mostly acoustic phonons,  $\kappa_a$  and  $\kappa_b$  show nearly identical cumulative values. They start to deviate from each other only when the phonon energy is higher than 15 meV, sampling into the optical phonon branches (Figure 4a). It can be also concluded from Figure 4b that optical phonon carried heat contributes to  $\kappa$  by  $\kappa_{\text{optical}}/\kappa \approx 34\%$  and 66% along the  $a$ - and  $b$ -axis, respectively.

The questions arising are then (1) why optical phonons contribute to  $\kappa$  by such an unusually high fraction in TiS<sub>3</sub> and (2) why such contribution differs so much for heat flowing along the  $a$ - and  $b$ -axis.

Crystals with complex unit cell structures have a large number of optical phonon modes, and they account for a high fraction of the phonon density of states. However, they typically contribute negligibly to thermal conductivity due to their low group velocities and short lifetimes.<sup>35</sup> In rare cases when optical phonons become dispersive with considerable group velocities, they may contribute significantly to the total thermal conductivity. For example, it has been recently shown that optical phonons account for 22% of  $\kappa$  in PbTe,<sup>36</sup> 25% in PbSe,<sup>36</sup> 30% in Mg<sub>2</sub>Si,<sup>37</sup> and 75% in hexagonal Ge<sub>2</sub>Sb<sub>2</sub>Te<sub>5</sub>.<sup>38</sup> We found that TiS<sub>3</sub> is another example for such a case. Figure

4a shows that between 10 and 30 meV, there exist a large number of dispersive optical phonon modes along both the  $a$ - and  $b$ -axis direction. Especially along the  $b$ -axis direction ( $\Gamma$ – $Z$ ), the optical phonon modes exhibit dispersions with a slope that is nearly parallel to those of the acoustic modes, indicating an unusually high optical phonon group velocity that is comparable to that of the acoustic phonons. The values of these velocities are compared in Table S1.

Following Mukhopadhyay et al.,<sup>38</sup> we calculated and show in Figure 4c the energy-dependent group velocity averaged over all phonon modes along the  $a$ - and  $b$ -axis directions. This averaged velocity is calculated by

$$\bar{v}(\omega) = \frac{(v^{\mu})^2(\omega)}{|v|} = \left(\frac{\Delta q}{2\pi}\right)^3 \sum_{\lambda} \frac{(v_{\lambda}^{\mu})^2}{|v_{\lambda}^{\mu}|} \delta(\omega - \omega_{\lambda}) / \sum_j g_j(\omega) \quad (2)$$

where  $v_j^{\mu}$  is the phonon group velocity of phonon mode  $j$  at wavevector  $\mathbf{q}$  along the  $\mu$ -axis and  $g_j(\omega)$  denotes phonon density of states. Two major features are evident from Figure 4c: (I) optical phonons (between 10–30 meV) exhibit considerable group velocity, comparable to that of acoustic phonons (between 0–15 meV), and (II) this effect is much more pronounced along the  $b$ - than  $a$ -axis direction, showing a high anisotropy attributed mostly to optical phonons, rather than acoustic phonons.

Effect I is related to the high dispersiveness of the optical phonons. In a simple 1D diatomic chain model,<sup>39</sup> a highly dispersive optical phonon mode requires strong intracell bonding and that the two atoms do not have extreme mass ratio. Contrasted to these, the acoustic phonon group velocity depends on intercell bonding and total mass in the unit cell. These conditions are all reasonably satisfied in TiS<sub>3</sub>. To have a high  $\kappa_{\text{optical}}/\kappa$ , it is also preferred that the contribution of acoustic phonons to  $\kappa$  ( $\kappa_{\text{acoustic}}$ ) is low. This is indeed the case in TiS<sub>3</sub>, where the acoustic phonons are expected to be scattered strongly via the three-phonon processes. The absence of bandgap between acoustic and optical phonons in Figure 4a facilitates the scattering of acoustic phonons by optical phonons (the so-called aao process, where “a” and “o” represent acoustic and optical phonons, respectively);<sup>40</sup> the well-separated (i.e., nonbunched) acoustic phonon lines provide large phase space for the scattering of acoustic phonons by each other (the so-called aaa process).<sup>40</sup> Taken together, these effects cause an unusually high  $\kappa_{\text{optical}}/\kappa$  in TiS<sub>3</sub>.

Effect II is attributed to the different bonding length and bonding configuration along the  $a$ - and  $b$ -axis crystallographic directions. As seen in Figure 4a, the optical phonon dispersions along the  $a$ -axis are in general flatter than along the  $b$ -axis, although several dispersive modes are also seen. This can be partially explained by the larger lattice constant, hence narrower Brillouin zone along the  $a$ -axis. Symmetry rules impose the requirement of zero slopes for these phonon modes at the zone center and boundary (e.g., at  $\Gamma$ ,  $Y$ , and  $Z$  in Figure 4a); therefore, a narrower zone would naturally lead to flatter optical bands and consequently lower optical phonon group velocities. This effect shares the same origin as in GaAs/AlAs superlattices,<sup>41</sup> where in the cross-plane direction GaAs and AlAs were grown in periods equal to  $n$  times the natural unit cell of their bulk counterparts. The Brillouin zone is then folded along the cross-plane direction to a width that is  $1/n$

Table 1. Comparison of Properties of Selected Materials<sup>a</sup>

		mass ratio, m/M	Debye temp (K)	max acoustic bandwidth, $\Delta_A$ (meV)	max optical bandwidth, $\Delta_O$ (meV)	$\kappa$ [W/(m K)], 300 K	$\kappa_{\text{optical}}/\kappa$ (%), 300 K	reference
TiS <sub>3</sub>	<i>b</i> -axis	0.67	438	20.9	14.0	5.78	66	this work
	<i>a</i> -axis		300	13.9	8.9	2.84	34	
	Si	1.0	710	51.1	18.2	145	5	Broido et al. <sup>34</sup>
	Ge	1.0	415	29.4	10.9	60	8	Broido et al. <sup>34</sup>
b-P	zigzag	1.0	278	24.0	9.2	30.1	27	Qin et al. <sup>43</sup>
	armchair			15.6	6.0	13.6	21	Qin et al. <sup>43</sup>
	PbSe	0.38	170	12.7	9.3	2.2	25	Tian et al. <sup>36</sup>
	PbTe	0.62	140	11.5	4.0	2.0	22	Tian et al. <sup>36</sup>
	Bi <sub>2</sub> Te <sub>3</sub> , in-plane	0.61	162	7.0	4.2	1.2	30	Hellman et al. <sup>44</sup>
	Ge <sub>2</sub> Sb <sub>2</sub> Te <sub>3</sub> , in-plane	0.58	100	5.8	7.1	1.7	75	Mukhopadhyay et al. <sup>38</sup>
	Mg <sub>2</sub> Si	0.86	432	35.2	14.0	11.3	30	Li et al. <sup>37</sup>
	Mg <sub>2</sub> Sn	0.20	273	14.6	8.3	7.2	18	Li et al. <sup>37</sup>
	SnSe, zigzag	0.66	210	6.9	6.7	2.0	61	Guo et al. <sup>45</sup>
	SnS, zigzag	0.27	270	8.0	10.0	2.3	70	Guo et al. <sup>45</sup>

<sup>a</sup> $\Delta_O$  and  $\Delta_A$  are bandwidths of the most dispersive optical and acoustic phonons from calculated dispersion relation.

times of the in-plane zone width, resulting in strong suppression of optical phonon group velocity in the cross-plane direction. A similar effect exists now along the *a*- and *b*-axis directions in TiS<sub>3</sub>, although both are in-plane. Aside from the high anisotropy in group velocity, optical phonons along these two directions do not differ much in their contribution to all three-phonon scattering processes. We calculated the relaxation lifetime of all three-phonon scattering processes, and the contributions to these processes from *a*- and *b*-axis optical phonons, and show the results in Figure S5. It can be seen that the optical phonons along these two directions do not differ significantly in their contribution to these processes. This finding further confirms the conclusion that it is the anisotropy in group velocity of the optical phonons, rather than their role in scattering acoustic phonons, that causes the large  $\kappa_b/\kappa_a$  in TiS<sub>3</sub>.

At the atomic scale, the strong in-plane anisotropy of thermal conductivity results from the distinct atomic bonding configurations. As shown in Figure 1, only two Ti–S bonds exist along the *a*-axis direction between any two Ti atoms, while there are six Ti–S bonds along the *b*-axis direction. Moreover, the strong anisotropy of optical phonons is reflected by the strong anisotropy of the electronic polarizability of TiS<sub>3</sub>. We calculated the Born effective charge  $(e^*)_{l,\mu\nu}$  of TiS<sub>3</sub>, which reflects the force of the atom *l* along  $\mu$ -direction, under the electric field along  $\nu$ -direction.<sup>42</sup> The diagonal components of the in-plane Born effective charge tensors are shown in Table S3, which shows that  $(e^*)_{bb}$  is much larger than  $(e^*)_{aa}$  for all Ti and S atoms. For example, for the Ti1(Ti2) and S3(S4) atoms, the ratio of  $(e^*)_{bb}/(e^*)_{aa}$  is 2–3, while for the atoms S1(S2) and S5(S6),  $(e^*)_{aa}$  are even smaller compared to  $(e^*)_{bb}$ . As is well-known, the optical modes correspond to the opposite displacement of positive and negative charged atoms, generating internal electric fields in the crystal. The magnitude of the restoration force of each atom depends on its Born effective charge. Consequently, the interactions along the *b*-axis will be stronger than those along the *a*-axis direction. The optical phonons are usually closely related to the dielectric permittivity. Therefore, it is expected that the dielectric constant would also be highly anisotropic in TiS<sub>3</sub>. Indeed, our DFT results show that the static dielectric constant in TiS<sub>3</sub>

are 12.51 and 33.15 along its *a*- and *b*-axis directions, respectively.

We also calculated the temperature dependence of  $\kappa$  along the two in-plane directions using DFT, including all possible phonon–phonon interactions but not phonon–impurity and phonon–boundary scatterings. As shown in Figure 3, although the values of the calculated  $\kappa$  are slightly higher than the measured values, their ratio,  $\kappa_b/\kappa_a$ , agrees well with the measurements.

We now compare all reported materials that show a high percentage of  $\kappa_{\text{optical}}/\kappa$  in an attempt to find properties in common. As seen from eq 1, it is not surprising that these materials typically have at least one optical phonon branch that is highly dispersive and thus has high group velocity to carry heat flow. The high dispersiveness would lead to large bandwidth for that phonon mode over the Brillouin zone. We define the normalized bandwidth ( $\Delta_O/\Delta_A$ ) as the bandwidth of the most dispersive optical phonon ( $\Delta_O$ ) divided by that ( $\Delta_A$ ) of the most dispersive acoustic phonon. In a simple diatomic chain model, a high  $\Delta_O/\Delta_A$  prefers similar masses of the two atoms, as well as stronger spring constant for vibration modes involving the lighter atoms than for the heavier atoms. From published calculated phonon dispersions of a selected set of materials including TiS<sub>3</sub> (Table 1), we plot in Figure 4d  $\kappa_{\text{optical}}/\kappa$  as a function of  $\Delta_O/\Delta_A$ . A positive correlation can be seen between these two quantities. The data scattering reflects factors missing in the plot: the lifetime ratio between optical and acoustic phonons differ in different materials, and only the single, most dispersive optical and acoustic phonons are considered. Nevertheless, the approximate correlation shows that optical phonons may contribute a large portion to lattice thermal conductivity in materials with one or more highly dispersive optical phonons. In TiS<sub>3</sub>, along *b*-axis more highly dispersive optical phonon branches with high group velocity contribute to carrying heat flow, leading to an unusually high portion of  $\kappa_{\text{optical}}/\kappa$ , as shown in Figure 4d.

In conclusion, we found an extreme anisotropy, by a factor of 2 and higher than that of any existing layered materials, in the in-plane thermal conductivity in TiS<sub>3</sub>. This occurs between the quasi-1D chain direction and the interchain direction in the basal plane of this layered material. First-principles calculations reveal that, unlike most materials where heat is mostly

transported by acoustic phonons, in  $\text{TiS}_3$  the optical phonons carry an unusually high portion of heat, up to 66% along the chain direction, owing to highly dispersive optical phonons. Perpendicular to the chain direction, however, the optical phonons are less dispersive and contribute to a much lower 34% of thermal conductivity. With such highly anisotropic thermal transport in the basal plane, layered  $\text{TiS}_3$  may serve as a platform for designing novel devices to route heat flow at the nanoscale, such as thermal switch, regulator, or diodes.<sup>46</sup>

## ■ ASSOCIATED CONTENT

### SI Supporting Information

The Supporting Information is available free of charge at <https://pubs.acs.org/doi/10.1021/acs.nanolett.0c01476>.

Experimental details, phonon dispersion and thermal properties, Born effective charge tensor; figures of optical images, electrical characterization, temperature dependence of  $\sigma$  and  $S$ , phonon dispersion, relaxation time vs optical phonon energy, Partial phonon density of states, Percentage of contribution to  $\kappa$ , electronic band structure, crystal structure, height profile, thermal conductivity, measured thermal conductance, and cumulative thermal conductivity vs phonon mean free path; tables of velocities, thermal conductivities, and Born effective charge tensors (PDF)

## ■ AUTHOR INFORMATION

### Corresponding Authors

**Junqiao Wu** – Materials Sciences Division, Lawrence Berkeley National Laboratory, Berkeley, California 94720, United States; Department of Materials Science and Engineering, University of California, Berkeley, California 94720, United States; [orcid.org/0000-0002-1498-0148](https://orcid.org/0000-0002-1498-0148); Email: [wuj@berkeley.edu](mailto:wuj@berkeley.edu)

**Jiawang Hong** – School of Aerospace Engineering, Beijing Institute of Technology, Beijing 100081, China; [orcid.org/0000-0002-9915-8072](https://orcid.org/0000-0002-9915-8072); Email: [hongjw@bit.edu.cn](mailto:hongjw@bit.edu.cn)

**Lidong Chen** – State Key Laboratory of High Performance Ceramics and Superfine Microstructure, Shanghai Institute of Ceramics, Chinese Academy of Sciences, Shanghai 200050, China; Email: [cld@mail.sic.ac.cn](mailto:cld@mail.sic.ac.cn)

### Authors

**Huili Liu** – Materials Sciences Division, Lawrence Berkeley National Laboratory, Berkeley, California 94720, United States; Department of Materials Science and Engineering, University of California, Berkeley, California 94720, United States; [orcid.org/0000-0001-8959-0315](https://orcid.org/0000-0001-8959-0315)

**Xiaoxia Yu** – School of Aerospace Engineering, Beijing Institute of Technology, Beijing 100081, China

**Kedi Wu** – School for Engineering of Matter, Transport, and Energy, Arizona State University, Tempe, Arizona 85287, United States; [orcid.org/0000-0003-4160-2457](https://orcid.org/0000-0003-4160-2457)

**Yang Gao** – Materials Sciences Division, Lawrence Berkeley National Laboratory, Berkeley, California 94720, United States; Department of Materials Science and Engineering, University of California, Berkeley, California 94720, United States

**Sefaattin Tongay** – School for Engineering of Matter, Transport, and Energy, Arizona State University, Tempe, Arizona 85287, United States; [orcid.org/0000-0001-8294-984X](https://orcid.org/0000-0001-8294-984X)

**Ali Javey** – Materials Sciences Division, Lawrence Berkeley National Laboratory, Berkeley, California 94720, United States; Department of Electrical Engineering and Computer Science, University of California, Berkeley, California 94720, United States; [orcid.org/0000-0001-7214-7931](https://orcid.org/0000-0001-7214-7931)

Complete contact information is available at:  
<https://pubs.acs.org/doi/10.1021/acs.nanolett.0c01476>

### Author Contributions

H.L. and J.W. conceived the project. H.L. designed the experiments, fabricated devices, and performed thermal and electrical measurements. X.Y. and J.H. performed the theoretical calculation. K.W. and S.T. provided the single crystal flake and SEM characterization of sample. H.L., X.Y., J.H. and J.W. discussed the data. H.L. and J.W. wrote the manuscript. All authors contributed to discussing the data and editing the manuscript.

### Author Contributions

<sup>#</sup>These authors contributed equally to this work.

### Notes

The authors declare no competing financial interest.

## ■ ACKNOWLEDGMENTS

This work was supported by the Electronic Materials Program at the Lawrence Berkeley National Laboratory, which is supported by the Office of Science, Office of Basic Energy Sciences, of the U.S. Department of Energy under Contract No. DE-AC02-05CH11231. J.H. acknowledges the support from the National Science Foundation of China (Grant No. 11572040), Beijing Natural Science Foundation (Grant No. Z190011), and the Technological Innovation Project of Beijing Institute of Technology. Theoretical calculations were performed using resources of National Supercomputer Center in Guangzhou. We thank Dr. Bin Chen for SEM characterization of sample. We thank Prof. Feng Wang and Dr. Saikat Mukhopadhyay for insightful discussions.

## ■ REFERENCES

- (1) Novoselov, K. S.; Geim, A. K.; Morozov, S. V.; Jiang, D.; Zhang, Y.; Dubonos, S. V.; Grigorieva, I. V.; Firsov, A. A. Electric field effect in atomically thin carbon films. *Science* **2004**, *306*, 666–669.
- (2) Castro Neto, A. H.; Guinea, F.; Peres, N. M. R.; Novoselov, K. S.; Geim, A. K. The electronic properties of graphene. *Rev. Mod. Phys.* **2009**, *81*, 109–162.
- (3) Mak, K. F.; Lee, C.; Hone, J.; Shan, J.; Heinz, T. F. Atomically thin  $\text{MoS}_2$ : a new direct-gap semiconductor. *Phys. Rev. Lett.* **2010**, *105*, 136805.
- (4) Deng, D.; Novoselov, K. S.; Fu, Q.; Zheng, N.; Tian, Z.; Bao, X. Catalysis with two-dimensional materials and their heterostructures. *Nat. Nanotechnol.* **2016**, *11*, 218–230.
- (5) Bonaccorso, F.; Sun, Z.; Hasan, T.; Ferrari, A. C. Graphene photonics and optoelectronics. *Nat. Photonics* **2010**, *4*, 611–622.
- (6) Wang, Q. H.; Kalantar-Zadeh, K.; Kis, A.; Coleman, J. N.; Strano, M. S. Electronics and optoelectronics of two-dimensional transition metal dichalcogenides. *Nat. Nanotechnol.* **2012**, *7*, 699–712.
- (7) Roy, K.; Padmanabhan, M.; Goswami, S.; Sai, T. P.; Ramalingam, G.; Raghavan, S.; Ghosh, A. Graphene- $\text{MoS}_2$  hybrid structures for multifunctional photoresponsive memory devices. *Nat. Nanotechnol.* **2013**, *8*, 826–830.
- (8) Britnell, L.; Ribeiro, R. M.; Eckmann, A.; Jalil, R.; Belle, B. D.; Mishchenko, A.; Kim, Y. J.; Gorbachev, R. V.; Georgiou, T.; Morozov, S. V.; Grigorenko, A. N.; Geim, A. K.; Casiraghi, C.; Castro Neto, A. H.; Novoselov, K. S. Strong light-matter interactions in heterostructures of atomically thin films. *Science* **2013**, *340*, 1311–1314.



- (9) Coleman, J. N.; Lotya, M.; O'Neill, A.; Bergin, S. D.; King, P. J.; Khan, U.; Young, K.; Gaucher, A.; De, S.; Smith, R. J.; Shvets, I. V.; Arora, S. K.; Stanton, G.; Kim, H.-Y.; Lee, K.; Kim, G. T.; Duesberg, G. S.; Hallam, T.; Boland, J. J.; Wang, J. J.; Donegan, J. F.; Grunlan, J. C.; Moriarty, G.; Shmeliov, A.; Nicholls, R. J.; Perkins, J. M.; Grievson, E. M.; Theuwissen, K.; McComb, D. W.; Nellist, P. D.; Nicolosi, V. Two-dimensional nanosheets produced by liquid exfoliation of layered materials. *Science* **2011**, *331*, 568–571.
- (10) Lee, S.; Yang, F.; Suh, J.; Yang, S.; Lee, Y.; Li, G.; Choe, H.; Suslu, A.; Chen, Y.; Ko, C.; Park, J.; Liu, K.; Li, J.; Hippalgaonkar, K.; Urban, J. J.; Tongay, S.; Wu, J. Anisotropic in-plane thermal conductivity of black phosphorus nanoribbons at temperatures higher than 100 K. *Nat. Commun.* **2015**, *6*, 8573.
- (11) Liu, H.; Choe, H. S.; Chen, Y.; Suh, J.; Ko, C.; Tongay, S.; Wu, J. Variable range hopping electric and thermoelectric transport in anisotropic black phosphorus. *Appl. Phys. Lett.* **2017**, *111*, 102101.
- (12) Chen, Y.; Chen, C.; Kealhofer, R.; Liu, H.; Yuan, Z.; Jiang, L.; Suh, J.; Park, J.; Ko, C.; Choe, H. S.; Avila, J.; Zhong, M.; Wei, Z.; Li, J.; Li, S.; Gao, H.; Liu, Y.; Analytis, J.; Xia, Q.; Asensio, M. C.; Wu, J. Black arsenic: a layered semiconductor with extreme in-plane anisotropy. *Adv. Mater.* **2018**, *30*, 1800754.
- (13) Zhao, L.-D.; Lo, S.-H.; Zhang, Y.; Sun, H.; Tan, G.; Uher, C.; Wolverton, C.; Dravid, V. P.; Kanatzidis, M. G. Ultralow thermal conductivity and high thermoelectric figure of merit in SnSe crystals. *Nature* **2014**, *508*, 373–377.
- (14) Son, Y.-W.; Cohen, M. L.; Louie, S. G. Energy gaps in graphene nanoribbons. *Phys. Rev. Lett.* **2006**, *97*, 216803.
- (15) Manzeli, S.; Ovchinnikov, D.; Pasquier, D.; Yazyev, O. V.; Kis, A. 2D transition metal dichalcogenides. *Nature Reviews Materials* **2017**, *2*, 17033.
- (16) Jin, Y.; Li, X.; Yang, J. Single layer of MX<sub>3</sub> (M = Ti, Zr; X = S, Se, Te): a new platform for nano-electronics and optics. *Phys. Chem. Chem. Phys.* **2015**, *17*, 18665–18669.
- (17) Island, J. O.; Biele, R.; Barawi, M.; Clamagirand, J. M.; Ares, J. R.; Sánchez, C.; van der Zant, H. S. J.; Ferrer, I. J.; D'Agosta, R.; Castellanos-Gomez, A. Titanium trisulfide (TiS<sub>3</sub>): a 2D semiconductor with quasi-1D optical and electronic properties. *Sci. Rep.* **2016**, *6*, 22214.
- (18) Gorlova, I. G.; Pokrovskii, V. Y.; Zybtev, S. G.; Titov, A. N.; Timofeev, V. N. Features of the conductivity of the quasi-one-dimensional compound TiS<sub>3</sub>. *J. Exp. Theor. Phys.* **2010**, *111*, 298–303.
- (19) Furuseth, S.; Brattaas, L.; Kjekshus, A. On the crystal structures of TiS<sub>3</sub>, ZrS<sub>3</sub>, ZrSe<sub>3</sub>, ZrTe<sub>3</sub>, HfS<sub>3</sub>, and HfSe<sub>3</sub>. *Acta Chem. Scand.* **1975**, *29*, 623–631.
- (20) Ferrer, I. J.; Ares, J. R.; Clamagirand, J. M.; Barawi, M.; Sánchez, C. Optical properties of titanium trisulphide (TiS<sub>3</sub>) thin films. *Thin Solid Films* **2013**, *535*, 398–401.
- (21) Kang, J.; Wang, L.-W. Robust band gap of TiS<sub>3</sub> nanofilms. *Phys. Chem. Chem. Phys.* **2016**, *18*, 14805–14809.
- (22) Lipatov, A.; Wilson, P. M.; Shekhirev, M.; Teeter, J. D.; Netusil, R.; Sinitskii, A. Few-layered titanium trisulfide (TiS<sub>3</sub>) field-effect transistors. *Nanoscale* **2015**, *7*, 12291–12296.
- (23) Island, J. O.; Barawi, M.; Biele, R.; Almazán, A.; Clamagirand, J. M.; Ares, J. R.; Sánchez, C.; van der Zant, H. S. J.; Álvarez, J. V.; D'Agosta, R.; Ferrer, I. J.; Castellanos-Gomez, A. TiS<sub>3</sub> transistors with tailored morphology and electrical properties. *Adv. Mater.* **2015**, *27*, 2595–2601.
- (24) Wu, K.; Torun, E.; Sahin, H.; Chen, B.; Fan, X.; Pant, A.; Wright, D. P.; Aoki, T.; Peeters, F. M.; Soignard, E.; Tongay, S. Unusual lattice vibration characteristics in whiskers of the pseudo-one-dimensional titanium trisulfide TiS<sub>3</sub>. *Nat. Commun.* **2016**, *7*, 12952.
- (25) Furuseth, S.; Fjellvåg, H.; Johansson, L.-G.; Gulyai, V. P.; Persson, I.; Elding, L. I. Re-examination of the crystal structure of ZrTe<sub>3</sub>. *Acta Chem. Scand.* **1991**, *45*, 694–697.
- (26) Fleet, M. E.; Harmer, S. L.; Liu, X.; Nesbitt, H. W. Polarized X-ray absorption spectroscopy and XPS of TiS<sub>3</sub>: S K- and Ti L-edge XANES and S and Ti 2p XPS. *Surf. Sci.* **2005**, *584*, 133–145.
- (27) Cordero, B.; Gómez, V.; Platero-Prats, A. E.; Revés, M.; Echeverría, J.; Cremades, E.; Barragán, F.; Alvarez, S. Covalent radii revisited. *Dalton Transactions* **2008**, 2832–2838.
- (28) Silva-Guillén, J. A.; Canadell, E.; Ordejón, P.; Guinea, F.; Roldán, R. Anisotropic features in the electronic structure of the two-dimensional transition metal trichalcogenide TiS<sub>3</sub>: electron doping and plasmons. *2D Mater.* **2017**, *4*, 025085.
- (29) Shi, L.; Li, D.; Yu, C.; Jang, W.; Kim, D.; Yao, Z.; Kim, P.; Majumdar, A. Measuring thermal and thermoelectric properties of one-dimensional nanostructures using a microfabricated device. *J. Heat Transfer* **2003**, *125*, 881–888.
- (30) Li, D.; Wu, Y.; Kim, P.; Shi, L.; Yang, P.; Majumdar, A. Thermal conductivity of individual silicon nanowires. *Appl. Phys. Lett.* **2003**, *83*, 2934–2936.
- (31) Lee, S.; Hippalgaonkar, K.; Yang, F.; Hong, J.; Ko, C.; Suh, J.; Liu, K.; Wang, K.; Urban, J. J.; Zhang, X.; Dames, C.; Hartnoll, S. A.; Delaire, O.; Wu, J. Anomalously low electronic thermal conductivity in metallic vanadium dioxide. *Science* **2017**, *355*, 371–374.
- (32) Hu, J.; Ruan, X.; Chen, Y. P. Thermal conductivity and thermal rectification in graphene nanoribbons: a molecular dynamics study. *Nano Lett.* **2009**, *9*, 2730–2735.
- (33) Zhang, J.; Liu, X.; Wen, Y.; Shi, L.; Chen, R.; Liu, H.; Shan, B. Titanium trisulfide monolayer as a potential thermoelectric material: a first-principles-based boltzmann transport study. *ACS Appl. Mater. Interfaces* **2017**, *9*, 2509–2515.
- (34) Broido, D. A.; Malorny, M.; Birner, G.; Mingo, N.; Stewart, D. A. Intrinsic lattice thermal conductivity of semiconductors from first principles. *Appl. Phys. Lett.* **2007**, *91*, 231922.
- (35) Ashcroft, N. W.; Mermin, N. D. *Solid State Physics*; Holt, Rinehart and Winston: New York, 1976.
- (36) Tian, Z.; Garg, J.; Esfarjani, K.; Shiga, T.; Shiomi, J.; Chen, G. Phonon conduction in PbSe, PbTe, and PbTe<sub>1-x</sub>Se<sub>x</sub> from first-principles calculations. *Phys. Rev. B: Condens. Matter Mater. Phys.* **2012**, *85*, 184303.
- (37) Li, W.; Lindsay, L.; Broido, D. A.; Stewart, D. A.; Mingo, N. Thermal conductivity of bulk and nanowire Mg<sub>2</sub>Si<sub>1-x</sub>Sn<sub>1-x</sub> alloys from first principles. *Phys. Rev. B: Condens. Matter Mater. Phys.* **2012**, *86*, 174307.
- (38) Mukhopadhyay, S.; Lindsay, L.; Singh, D. J. Optic phonons and anisotropic thermal conductivity in hexagonal Ge<sub>2</sub>Sb<sub>2</sub>Te<sub>5</sub>. *Sci. Rep.* **2016**, *6*, 37076.
- (39) Kittel, C. *Introduction to Solid State Physics*, 7th ed.; Wiley: New York, 1996.
- (40) Lindsay, L.; Broido, D. A.; Reinecke, T. L. First-principles determination of ultrahigh thermal conductivity of boron arsenide: a competitor for diamond? *Phys. Rev. Lett.* **2013**, *111*, 025901.
- (41) Bies, W. E.; Radtke, R. J.; Ehrenreich, H. Phonon dispersion effects and the thermal conductivity reduction in GaAs/AlAs superlattices. *J. Appl. Phys.* **2000**, *88*, 1498–1503.
- (42) Gonze, X.; Lee, C. Dynamical matrices, Born effective charges, dielectric permittivity tensors, and interatomic force constants from density-functional perturbation theory. *Phys. Rev. B: Condens. Matter Mater. Phys.* **1997**, *55*, 10355–10368.
- (43) Qin, G.; Yan, Q.-B.; Qin, Z.; Yue, S.-Y.; Hu, M.; Su, G. Anisotropic intrinsic lattice thermal conductivity of phosphorene from first principles. *Phys. Chem. Chem. Phys.* **2015**, *17*, 4854–4858.
- (44) Hellman, O.; Broido, D. A. Phonon thermal transport in Bi<sub>2</sub>Te<sub>3</sub> from first principles. *Phys. Rev. B: Condens. Matter Mater. Phys.* **2014**, *90*, 134309.
- (45) Guo, R.; Wang, X.; Kuang, Y.; Huang, B. First-principles study of anisotropic thermoelectric transport properties of IV-VI semiconductor compounds SnSe and SnS. *Phys. Rev. B: Condens. Matter Mater. Phys.* **2015**, *92*, 115202.
- (46) Wehmeyer, G.; Yabuki, T.; Monachon, C.; Wu, J.; Dames, C. Thermal diodes, regulators, and switches: physical mechanisms and potential applications. *Appl. Phys. Rev.* **2017**, *4*, 041304.